Stroboscopic Ultrafast Imaging Capabilities Using RF Strip-lines in a Commercial Transmission Electron Microscope

Spencer A. Reisbick[1], Myung-Geun Han[1], Chuhang Liu[1,3], Yubin Zhao[2], Eric Montgomery[2], Vikrant J. Gokhale[4], Jason J. Gorman[5], Chunguang Jing[2], June W. Lau[6] and Yimei Zhu[1,*]

[1]*Condensed Matter Physics and Materials Science Department, Brookhaven National Laboratory, Upton, NY 11973, USA*

[2]*Euclid Techlabs LLC, 365 Remington Blvd. Bolingbrook, IL 60440, USA*

[3]*Department of Physics and Astronomy, Stony Brook University, Stony Brook, NY 11794, USA*

[4]*Microsystems and Nanotechnology Division, National Institute of Standards and Technology, Gaithersburg, MD 20899, USA.*

[5]*U.S. Naval Research Laboratory, Washington, DC,20003 USA*

[6]*Materials Science and Engineering Division, National Institute of Standards and Technology, Gaithersburg, MD 20899, USA.*

Abstract: The development of ultrafast electron microscopy (UEM), specifically stroboscopic imaging, has brought the study of structural dynamics to a new level by overcoming the spatial limitations of ultrafast spectroscopy and the temporal restrictions of traditional TEM simultaneously. Combining the concepts governing both techniques has enabled direct visualization of dynamics with spatiotemporal resolutions in the picosecond-nanometer regime. Here, we push the limits of imaging using a pulsed electron beam *via* RF induced transverse deflection based on the newly developed 200 keV frequency-tunable strip-line pulser. We demonstrate 0.2 nm spatial resolution at high magnifications and elucidation of Lorentz imaging using the phase-microscopy method. We also present beam coherence measurements and expand our study using the breathing modes of a silicon interdigitated comb under RF excitation which achieves improved temporal synchronization between the electron pulse-train and electric field. A new RF holder has also been developed with impedance matching to the RF signal to minimize transmission power loss to samples and its performance is compared with a conventional sample holder.

Keywords: Ultrafast electron microscopy, electron pulser, frequency-tunable RF excitation, time-resolved stroboscopic imaging, coherent electron pulses.

1. INTRODUCTION

Atomic imaging *via* transmission electron microscopy (TEM) has become a powerful characterization technique due to aberration correction and direct electron detection [1–4]. The technique is widely used for materials characterization because of its ability to elucidate crystallographic and compositional structures of single-particles [5–8]. Traditionally, the electron beam is continuous with a pseudo-random emission profile on the specimen. As a result, typical temporal resolutions of conventional electron microscopy are limited to a few milliseconds due to the frame rate of the detector [9–11]. These domains enable dynamic observation of slow *in situ* processes such as Avrami crystallization and biological degradation [12–14]. However, complex magnetic and electronic dynamics can occur in the sub-picosecond regime [15–18].

Ultrafast electron microscopy (UEM) has been developed to elucidate nanometer scale structural dynamics occurring in their native temporal domains. UEM's unique ability to image in this exclusive spatiotemporal domain is particularly relevant to some of the most interesting challenges posed by quantum information science. Specifically, qubit devices can transmit data at 5 GHz operation frequencies, which were not identified without large spatial resonance techniques, until recently [19,20]. Alternative mechanisms for data transmission are also emerging, although the fundamental processes are not completely understood [21,22]. The development of UEM enables the exploration of nanoscale processes on femtosecond temporal and nanometer spatial scales simultaneously [23,24]. Operation is predicated on a pseudo-binary distribution of electron-specimen interactions through beam blanking or laser illumination [25]. Laser-based techniques are the most frequent form of electron pulse generation in UEM because of the resemblance to ultrafast spectroscopy. However, barriers to the widespread use of femtosecond lasers include cost, placement and microscope modifications during the initial startup. More importantly, laser-induced thermal heating and the difference in penetration depth between the photon-pump and electron-probe at the sample creates additional complications in data analysis and interpretation.

The Euclid Techlabs' UltraFast Pulser[1] (hereafter referred to as the pulser) is an alternative to laser-based UEM [26–28]. As shown in Fig. 1, the electron beam enters an RF strip-line (K1) which sweeps it laterally across a beam chopping aperture (BCA). Short electron pulses transmit through the aperture with a large momentum distribution, then enter a second RF strip-line (K2) designed to demodulate the momenta dispersion to the original state. Fractional amounts of electrons transmit through the BCA forming pulses as small as 10 ps that are tunable *via* the sweeping frequency, BCA diameter and applied voltage across K1 [26–28]. Placing the pulser downstream from the gun chamber retains the original emission making it the largest advantage of RF strip-line technology in UEM. Without the complication of lasers and their associated optics, conventional TEM modalities are easily recovered by removing the applied potential across both strip-lines and retracting the BCA. Unfortunately, current state-of-the-art RF technology does not have a large range of pulse durations like laser-based techniques, so there is still room for improvement.

Here, we demonstrate quantitative comparisons between continuous and pulsed electron

[1] Certain commercial equipment, instruments, or materials are identified in this presentation to specify the experimental procedure adequately. Such identification is not intended to imply recommendation or endorsement by the National Institute of Standards and Technology, nor is it intended to imply that the materials or equipment identified are necessarily the best available for the purpose.

beams *via* the pulser installed on a modified commercial electron microscope. We evaluate a myriad of common electron microscopy techniques and quantify their ability to retain feature contrast. The microscope has been modified from previous work by replacing its original field-free polepiece with a high-resolution polepiece to improve spatial resolution [26–28]. Additionally, we have implemented a new alignment technique between K1 and K2 with additional grounding to prevent charging. As a result, we resolve 0.2 nm lattice fringes and elucidate phase images of magnetic domains for the first time using picosecond electron pulses [29–32]. Further, we find anisotropic retention of the coherence through classic Fresnel fringe measurements that aligns directionally with the sweeping motion of the electron beam [33]. We also demonstrate a new RF compatible holder with improved power transmission and explore the intricate imaging conditions and optimization of an interdigitated silicon comb for time-resolved experiments [26–28].

2. MATERIALS AND METHODS

2.1 Electron Microscopy Data Acquisitions

Electron micrographs were acquired using a TEM operated at 200 kV with the pulser inserted directly below the field-emission electron gun. Explanation of physical connections and general operation can be found elsewhere [26–28]. The relevant aperture sizes, RF sweeping frequency and K1/K2 modulation and demodulation parameters for all images are provided in Table S1. Images were acquired using a commercial 4-megapixel electron camera. A software control interface was used to control the applied voltages and phase applied to K1 and K2. All specimens, except for the evaporated permalloy (Py) film, were calibration standards.

2.2 Evaporated Permalloy Sample Preparation

A Py film was evaporated over a 2000 mesh copper grid onto a 100 µm x 100 µm x 10 nm silicon nitride (SiN) window while taped to an aluminum foil platform in a home-built film evaporator. The electron gun was run at nominal 80 µA until the sample reached an approximate thickness of 20 nm. The 2000 mesh copper grid was removed leaving the SiN window with Py squares nearly 6.5 µm x 6.5 µm in size with a 4 µm lateral separation.

2.3 Holder Transmission Measurements

Power transmission through the RF compatible TEM holder was measured *via* the S_{21} transmission signal using a network analyzer. The signal was passed from the network analyzer to the holder without a sample to measure only the losses of the holder. A high frequency probe was connected to the signal line on the printed circuit board (PCB) carrier shown in Figure 6.

3. RESULTS AND DISCUSSION

3.1 Installation comparison of the ultrafast pulser

Recent advancements in UEM have enabled direct visualization of materials responses on their native time scales [34–42]. The pulser can quickly change its operation mode between a continuous and pulsed electron beam with minimal tuning of the microscope optics. Three primary modifications to the microscope and pulser have improved the imaging capabilities. The alignment procedure between K1 and K2 has been improved such that the center of the pulser is easier to align along the optic axis of the microscope. Lead shielding around the deflection cavity has also been employed to prevent charging from electrons scattering off the BCA. Lastly, we have inserted a 0.23 nm point-to-point high-resolution pole piece to improve the spatial resolution. Figure 1 contains a schematic of the components used to modulate and demodulate the beam to pulse the electron beam. After exiting the gun assembly, the electron beam enters K1 and is laterally swept across the BCA, chopping it into pulses with picosecond duration that enter K2. K2 demodulates the electron pulses with an RF field 180° out-of-phase from K1 before transmitting them to the traditional lens system of the TEM. Figure 1c demonstrates the quality of the electron beam in continuous and pulsed operation. Each measured parameter was extracted by fitting the beam profile to an error function (See Figure S1). The pulser increases the distance between the electron cathode and condenser aperture by about 0.5 m, so we have checked the retention of electron counts before and after installation (Figure 1d). The maximum beam currents were not compromised due to the installation of the pulser at the sample and subsequent detectors when the microscope is used conventionally. More information regarding the methodology and specific measurements can be found in Figure S1.

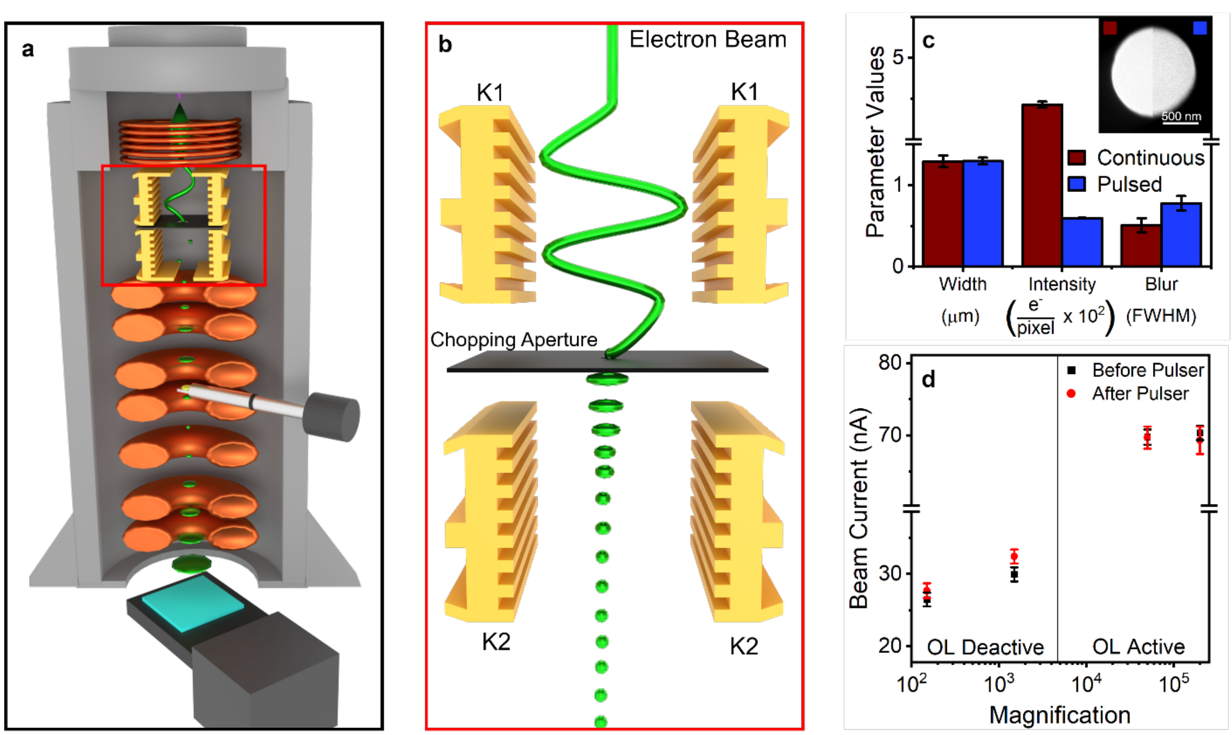

Figure 1. Illustration of the pulser installation on a TEM. (a) Schematic of a traditional TEM with the pulser inserted below the cathode as indicated by the red box. (b) Magnified and exaggerated rendering of the pulser components used for modulation (K1) and demodulation (K2) of the electron beam. The electron beam is swept by K1 over a BCA to generate pulses. Electron pulses drift with dispersed momenta directions, so K2 demodulates them through a time-dependent RF field, locked at 180° with respect to K1. (c) Comparison of the electron beam in continuous and pulsed operation using the fitting parameters to an error function (see Figure S1). The width and intensity refer to the diameter and number of electrons in the beam, respectively. The blurriness of the beam edge was measured using the FWHM. The inset contains micrographs of the continuous (left) and pulsed (right) beams for comparison. Error bars are the standard deviation of triplicate measurements for each fit parameter. (d) Comparison of the electron beam intensity at different magnifications before and after pulser installation using an illumination about 5 cm. Quantitative comparisons are only to demonstrate that analogous beam currents are achievable with the pulser modification. Error bars are the standard deviation of triplicate measurements over different days before and after installation.

Two of the most important capabilities of the pulser is the quality of the pulsed electron beam and retention of conventional TEM performance. Upon activation of the sweeping mechanisms in K1 and K2, the width of the beam is not affected, indicating that demodulation is effective. However, the intensity in the electron beam drops by 75 % to 90 % depending on the RF voltage and sweeping frequency (duty cycle) applied to K1. Reducing the BCA diameter produces shorter electron pulses, but loses signal, requiring a compromise between temporal duration and image intensity. Modulation of the electron beam induces a transverse broadening of the electron beam which is mostly corrected using K2 as shown by the full width at half-maximum (FWHM) of the intensity rise of the beam. When the beam is continuous, edges are sharper because the electron beam is not being modified. The pulser intentionally moves the electron beam off-axis and compensates for most of the modulation, but still contains a slight distortion. The beam currents are comparable before and after installation when the pulser electronics remain off. The quantity of electrons reaching the detector is maintained regardless of the additional ≈0.5 m drift space between the exit of the gun chamber and first condenser lens. Note that previous publications using the pulser were based on a low-excitation, magnetic field free objective lens pole piece rather than the high-resolution pole piece used here [26–28]. Specifically, this pole piece has a 0.23 nm nominal point to point resolution and a tilt range ±40° and ±30° for the α and β directions, respectively. The work presented here examines techniques including Fresnel and high-resolution imaging in addition to traditional bright field and diffraction. After installation of the high-resolution pole piece, the gun and lens operating conditions were optimized, so quantitative comparison of the beam currents is not as important as the ability to maintain prior electron quantities for imaging.

3.2 Standard imaging capabilities using the ultrafast pulser

The most common imaging techniques in traditional TEM for materials characterization purposes are bright field imaging and diffraction. We imaged gold nanoparticles deposited on holey carbon film as shown in Figure 2a and 2b with continuous and pulsed beams, respectively. We have intentionally induced vertical astigmatism in the images to quantitatively compare distortions in the imaging conditions. Figure 2c contains the respective diffraction patterns (DP) of the gold nanoparticles where the contrast of the pulsed electron beam has been enhanced to demonstrate that six diffraction rings are visible in both operation modes. Figures 2d, 2e and 2f provide quantitative comparisons of the bright field and diffraction images using the pulser. In bright field imaging, the intensity, contrast and sharpness correspond to the total electrons, local gradient of the intensity and width of the gradient (See Figure S2), respectively. In diffraction, the spacing and width were measured by fitting the radially averaged (220)-peak (0.143 nm) to a Gaussian (See Figure S2). The (220) peak was selected for fitting purposes because it is spatially isolated, even though higher order planes are visible. Radial integration of the diffraction patterns is provided in Figure 2e with each set of planes labeled. Note that there is a large disparity between the intensity of the continuous and pulsed electron beams, so each integration has been normalized and offset to demonstrate the shape.

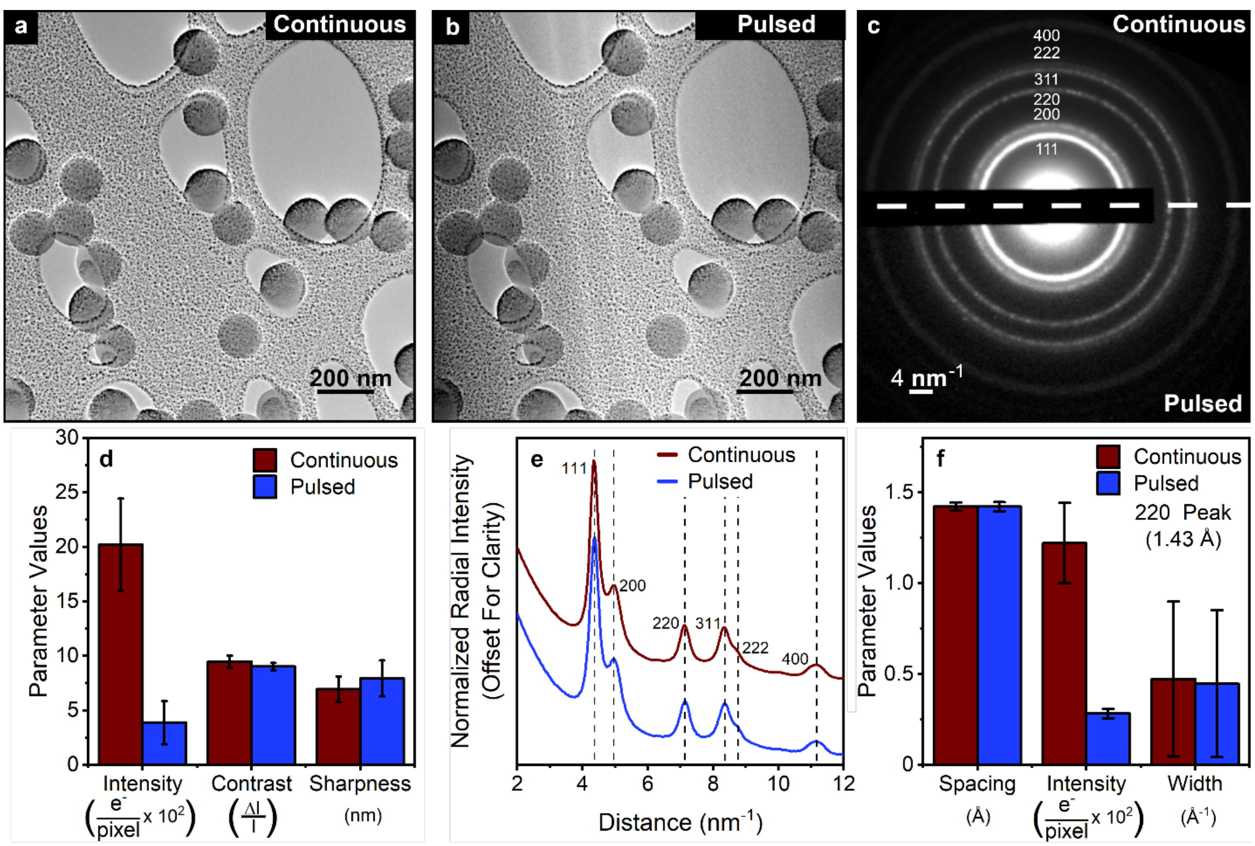

Figure 2. Demonstration of bright field and diffraction capabilities using the pulser. (a, b) Bright field images of gold nanoparticles on holey carbon using continuous (a) and pulsed (b) electron beams with 5 s same acquisition times. (c) Diffraction patterns from (a) and (b) with the planar reflections for gold indicated for a continuous (top) and pulsed (bottom) electron beam. (d) Quantitative comparison of the bright field images in (a) and (b). Intensity refers to the average number of electrons collected such that the ratio between the two is equal to the duty cycle of the pulsed beam (≈20 %). Contrast and sharpness refer to the intensity magnitude change and width along intentionally bright astigmatic boundaries (see Figure S2). Error bars are the standard deviation of triplicate measurements at different sample locations. (e) Normalized radial integrations of the DP intensity profile in (c). Note the intensity disparity is nearly five-fold, so the vertical axis has been normalized to demonstrate the curve shape rather than the amplitude. (f) Quantitative comparison of the (220)-peak for each radially integrated intensity profile. The d-spacing, intensity and width refer to the position, amplitude and FWHM of a Gaussian fit. Error bars are the standard error for each fitting parameter.

Image differences in bright field and diffraction are qualitatively undetectable between continuous or pulsed operation of the pulser. The main difference is the reduction of electron counts due to the removal of many off-axis electrons by the BCA. This can be corrected by longer acquisition times but requires increased stability of the probe and specimen. Quantitatively, the resolution, contrast, and position of features are all retained within statistical error. The most important aspect in imaging with the new pulser system is that the images are not altered by the imposed sweeping motion of the RF field. Here, we verify that the modulation of the electron beam is sufficiently corrected to retain the original images and corresponding quantitative information. The intensity is reduced by nearly 80 % during pulsed operation, so acquisitions require five times longer to achieve similar counts. Specimen stability at very low magnifications is typically not an issue, so decreasing the K1 sweeping voltage or increasing the RF frequency is an alternative to increase the quantity of electrons reaching the sample. Increases in the BCA diameter also allows increased electron transmission at the cost of a higher duty cycle. Consequently, each of these adjustments decrease the pulse duration which becomes important for time-resolved dynamic analysis.

To test the magnetic imaging capabilities of the pulser we used Lorentz phase transmission electron microscopy (LTEM) *via* Fresnel contrast [31]. In phase microscopy, magnetic moments in the sample deflect transmitted electrons when the beam is not at focus. The deflection angle and subsequent amplitude increases as the magnitude of defocus is increased. Spin-induced deflection of incident electrons is equivalent to the change of phase of the electron wavefront in a quantum mechanical description. In Figure 3, we present magnetic vortex states in evaporated 6.5 μm Py squares with the corresponding difference, phase and induction maps for continuous and pulsed electron beams [43,44]. Over- and under- focused images were acquired ≈3.1 mm away from eucentric focus. The phase of the square element was retrieved using the transport-of-intensity (TIE) method through standard reconstruction procedures [45–47]. We note sufficient stability to detect ripple contrast in the polycrystalline Py elements due to its magnetocrystalline anisotropy. Line profiles of the vortex-cores and the subsequent Gaussian fits (Figure S3) suggest there is no difference in spatial resolution of the Lorentz imaging using continuous and pulsed beams. The phase and corresponding induction maps correspond demonstrate the reconstructed magnetic spin directions in the Py sample.

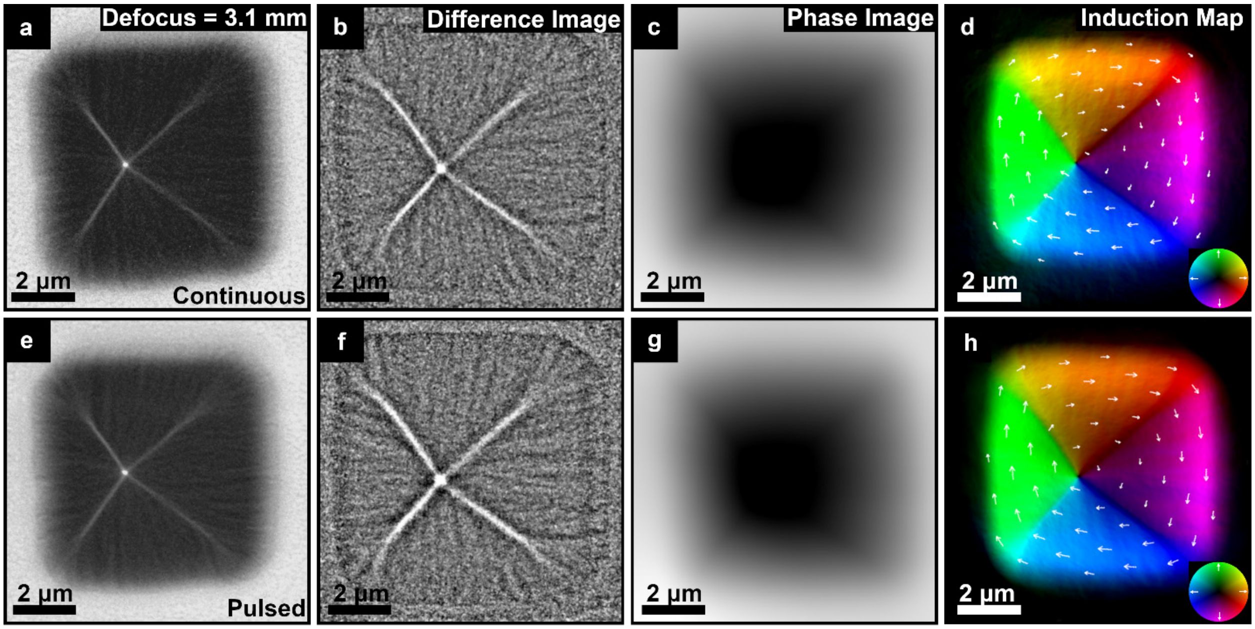

Figure 3. Demonstration of LTEM using a 6.5 μm Py square during operation of the electron pulser. (a, e) Py square imaged using continuous (a) and pulsed (e) electron beams at a defocus of ≈3.1 mm. Images are adjusted to similarly represent the intensity. (b, f) Difference between over- and under-focused images after alignment. (c, g) Phase images constructed from the alignment of over- and under- focused LTEM images. (d, h) Induction maps, or vector maps, based on TIE analysis showing the reconstructed spin arrangement. The color and brightness correspond to the in-plane spin direction and amplitude, respectively (see color-wheel legend at the right-bottom corner). The spin directions are also shown as arrows overlayed on the color map. Quantitative comparisons in the same format of the other figures in this paper are provided in the Supplementary Information.

Since LTEM requires a defocused electron beam to detect the phase of the electron wave front passing through a sample, a Py square with the magnetic Landau structure (vortex core with four 90° domain walls) was used to test whether the pulser would be able to retain electron phase information qualitatively and quantitatively. Qualitatively, spin reconstructions using the TIE retrieval method show minimal differences in retrieval of the magnetic signals. Quantitative analysis confirms that the primary difference in operation lie in the intensity of the acquisition and the necessary collection times. The ≈80 % intensity reduction agrees with bright field imaging for similar K1 voltages and chopping apertures. Furthermore, the sharpness of the vortex center using a pulsed beam now lies within statistical error of the continuous beam. The presence of magnetic domains amplifies the effects of modulated electrons, meaning significant improvements in demodulation can be achieved using phase imaging techniques. Recall that the K1 sweeping motion induces two electron packets of unique momenta *via* the forward and backward propagation across the chopping aperture. Improper demodulation manifests as double images due to the inverse momentum vectors and is amplified when the beam is defocused. The dispersion amplification acts to assist in more precise demodulation because of the oppositely dispersed electron packets.

At low magnifications, the continuous and pulsed electron beams yield almost no differences when imaging the sample because the alignments are not as sensitive to demodulation. Ideally, pulsed electron beams would retain the best achievable spatial resolution compared to the continuous counterpart. In fact, 500 μs pulses extracted *via* laser-induced beam amplification can improve the spatial resolution [48]. The long pulse durations and amplification allows retention of the intensity of the continuous and pulsed beams. However, microsecond pulses do not accommodate the need to achieve sub-picosecond temporal resolution. Figure 4 contains images using picosecond electron pulses to resolve 0.2 nm lattice fringes (corresponding to the 200 reflection) in gold nanoparticles using a 0.23 nm point-to-point high-resolution pole-piece. Specifically, we resolve multiple domains within a single nanoparticle as shown in Figure 4b. It should be noted that switching between continuous and pulsed operation at high magnifications requires different lens alignments. As well, the objective and condenser lens astigmatism alignments require additional tuning due to the elongation of the electron beam in K1. To correct for imperfections in demodulation, intentional astigmatism was introduced to correct an induced spherical aberration caused by the sweeping motion. The insets of Figure 4 contain a comparison of the FFT spectra when using continuous and pulsed electron beams to demonstrate the quantitative consistency between high resolution images. Further, Figure 4f quantitively compares the contrast, d-spacing and total dose for each acquisition. Note that the pulsed acquisition has been lengthened to approximately match the total quantity of electrons arriving at the sample (≈450 electrons per pixel).

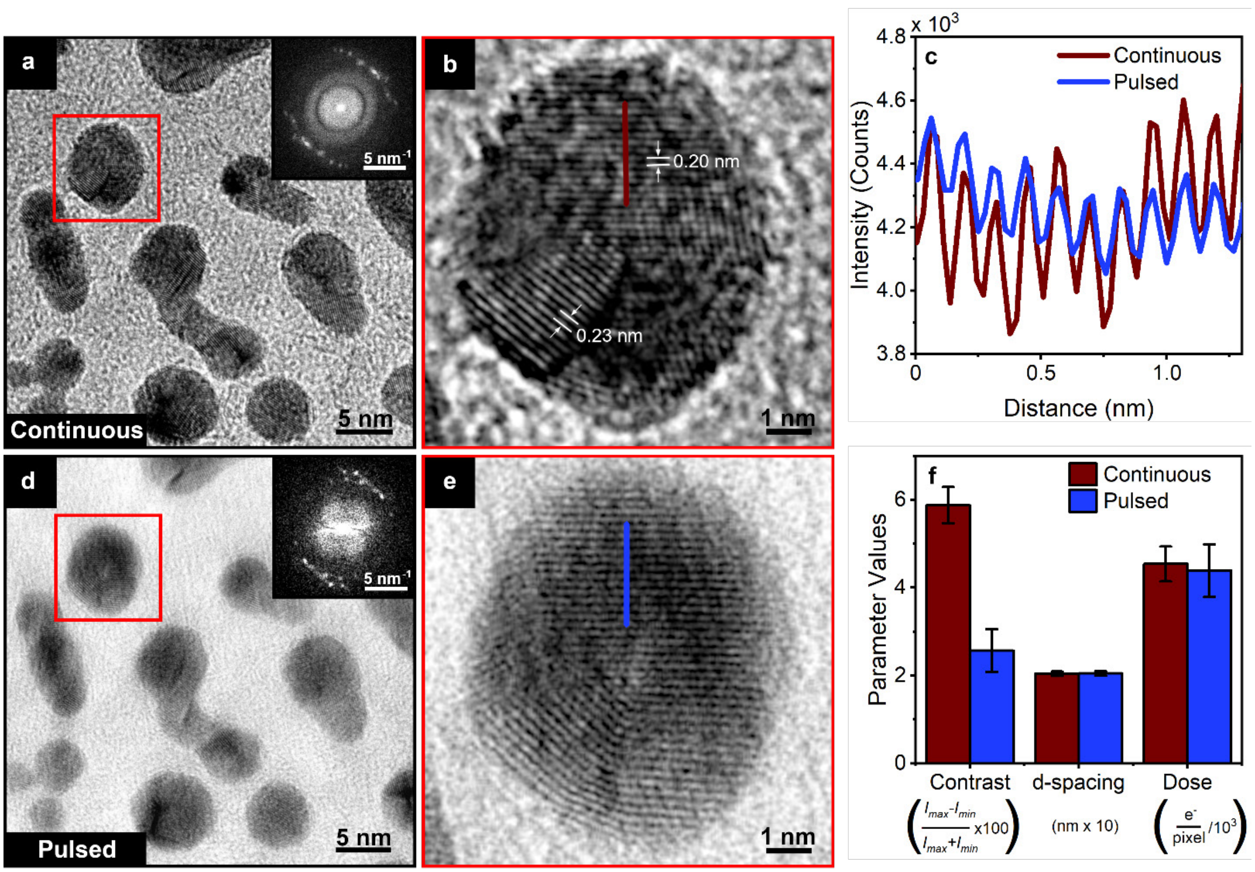

Figure 4. High-resolution imaging of gold nanoparticles using continuous and pulsed electron beams. (a, d) Bright field images of gold nanoparticles using continuous (a) and pulsed (d) electron beams without an objective aperture. (b, e) Magnified images from the regions-of-interest in (a) and (d). Pulsed beam images were acquired longer to achieve similar total doses to ensure that fringe visibility was not affected by signal reduction. (c) Intensity line profiles taken from (b) and (e) along the respective ROIs. (f) Quantitative comparison of the contrast, lattice spacing and accumulated dose using the continuous (maroon) and pulsed (blue) electron beams measured from the line profiles in (c).

At higher magnifications, the differences between the continuous and pulsed electron beams are more apparent, primarily due to the disparity in electron counts. However, the magnitude of the FFT peaks and corresponding lattice spacing are unaltered when imaged with the pulsed electron beam. We have noticed that the sensitivity of lattices spacings oriented relative to the sweeping direction of the beam are correlated. Currently, any deviation between the alignment of crystallographic planes and electron beam motion causes anisotropic resolution reduction and requires additional tuning of the electron beam. We believe that additional tuning the internal alignments of the pulser will further enhance the spatial resolution. Secondly, similar electron counts for the pulsed beam image required a longer acquisition and more converged beam, causing additional aberrations in the image. We have implemented both techniques to achieve similar dose quantities in the continuous and pulsed images to prevent time-dependent specimen drift. Due to the balance between acquisition time and sufficient SNR there are still improvements that are being implemented to the pulser but have provided evidence of the substantial improvement.

3.3 Modulated pulsed electron beam coherence using the ultrafast pulser

We further evaluate the beam coherence and its importance for phase imaging such as Lorentz microscopy and holography as tools for quantum information science. Here, we demonstrate anisotropic retention of the electron beam coherence by imaging Fresnel fringes from a 5 μm hole in a SiN substrate [49]. Because the hole is round, we can evaluate the coherence with a 360° angular distribution relative to the beam sweeping direction. Figure 5 contains the respective Fresnel fringes for a continuous and pulsed electron beam with two orthogonal directions indicated. Figures 5c and 5f contain line profiles parallel (1) to and perpendicular (2) the beam sweeping direction as a comparison of the anisotropy. Here, the quantity of fringes directly corresponds to the translational coherence of the beam and the effective size of the initial source [50,51].

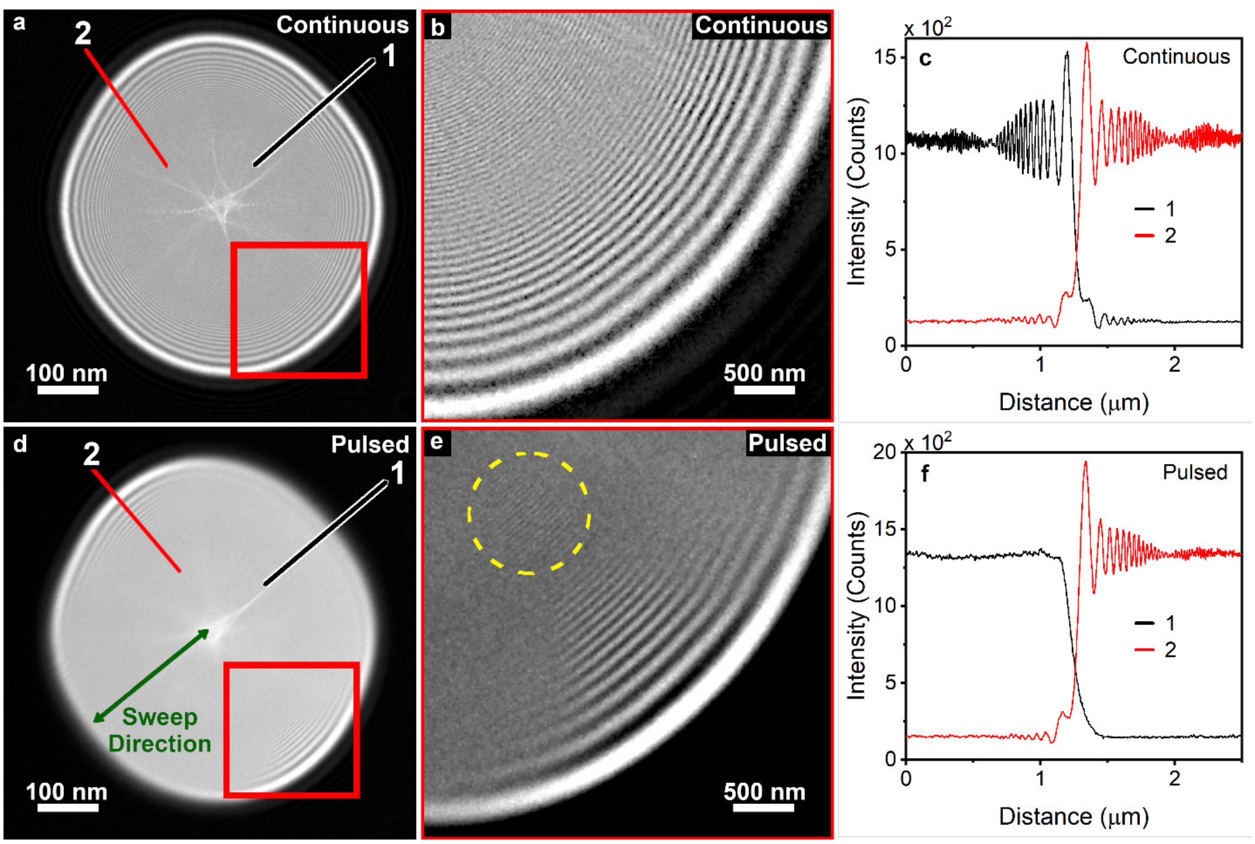

Figure 5. Anisotropic electronic beam coherence using the RF pulser on a round SiN window. (a, d) Defocused image (-11 mm) image of a round SiN window acquired using a continuous (a) and pulsed (d) electron beam. The directions parallel (1) and perpendicular (2) to the beam sweep direction (green arrow) have been indicated. Note that the accumulated acquisition time for the continuous and pulsed images are 20 s and 90 s, respectively, causing the latter to appear brighter (duty cycle of 40 %). (b, e) Magnified images from the ROIs in (a) and (d) to enhance the quantity of visible Fresnel fringes. The brightness and contrast in (e) have been modified to amplify the appearance of the fringes at the cost of other features. The yellow circle contains higher order Fresnel fringes during the pulsed acquisition which are oriented parallel to the beam sweeping direction. (c, f) Anisotropic line profiles laying parallel (black) and perpendicular (red) to the beam sweeping direction showing the coherence during continuous (c) and pulsed (f) operation.

During pulsed operation, the Fresnel fringes at the edges of the SiN window parallel to the sweeping direction of the electron beam retain their visibility more than those perpendicular. In fact, fringes aligned perpendicular to the beam sweeping direction are almost entirely unresolvable. In Figure 5d, the translational coherence is isotropic during continuous beam operation with fringes reaching the spatial limitations of the camera. Note that the quantity and clarity of the fringes do not change with respect to the angular component from the center of the SiN hole. Changing to a pulsed electron beam reduces the coherence anisotropically due to the modulation of the electron beam along one direction. Consequently, the parallel and perpendicular translational coherences relative to the beam sweeping direction is reduced and maintained, respectively. Ideally, demodulation would return the electron pulses back to the original size and momentum of the continuous beam, so there is room for improvement in this evaluation. The translational coherence of the electron beam is radially dependent on the beam sweep direction, so it is promising that directional phase methods (*i.e*. Holography) can be accomplished using this quality. Further, smaller chopping apertures (currently limited to 25 μm) would reduce the momenta distribution of the electron beam exiting K1, which would simplify in K2 demodulation and potentially improve the data quality.

3.4 Development of a new RF compatible holder for use with the ultrafast pulser

The purpose of the development of the electron pulser is to conduct laser free ultrafast experiments under RF excitation, which has the potential to provide direct observations of qubit or high-speed devices at 4 K *in operando*. Among the challenges we are facing, the sample holder must be compatible with the RF signal and have minimal power losses. We have developed a new sample holder (Fig.6a) that is impedance matched to yield improved signal transmission to the sample by introducing a vacuum compatible RF transmission line capable of operating at frequencies greater than 0.5 GHz. In previous experiments, the maximum transmission (above 0.5 GHz) was near 40 %, then dropped below 5 % at 3.5 GHz [26–28]. The RF input is connected *via* an SMA connection located on the rear of the holder. This signal line travels down the center of the holder architecture and exits as a wire near the normal position of the sample. We have also designed interchangeable PCB chip carriers that are easily inserted into contact with the signal line through a screw-based clamping mechanism (See supplementary information). In Figure 6a, the PCB has signal and ground lines passing through the center and edges of the board, respectively. The sample is mounted in a standard 3 mm opening that splits the signal line. Bonding is required to electrically connect the sample to the signal line on the PCB carrier chip. To test the holder, we replicated electrostatic breathing modes in an interdigitated comb using an RF input power of ≈0.5

W (comparable to previous magnitudes) [27]. We previously did not discuss the effect of defocus on breathing modes in the interdigitated comb structure. Electrostatic breathing modes are amplified using a largely under- or over-focused electron beam. However, focusing electron beam does not deflect the electrons enough to measure any modulation in the tine widths.

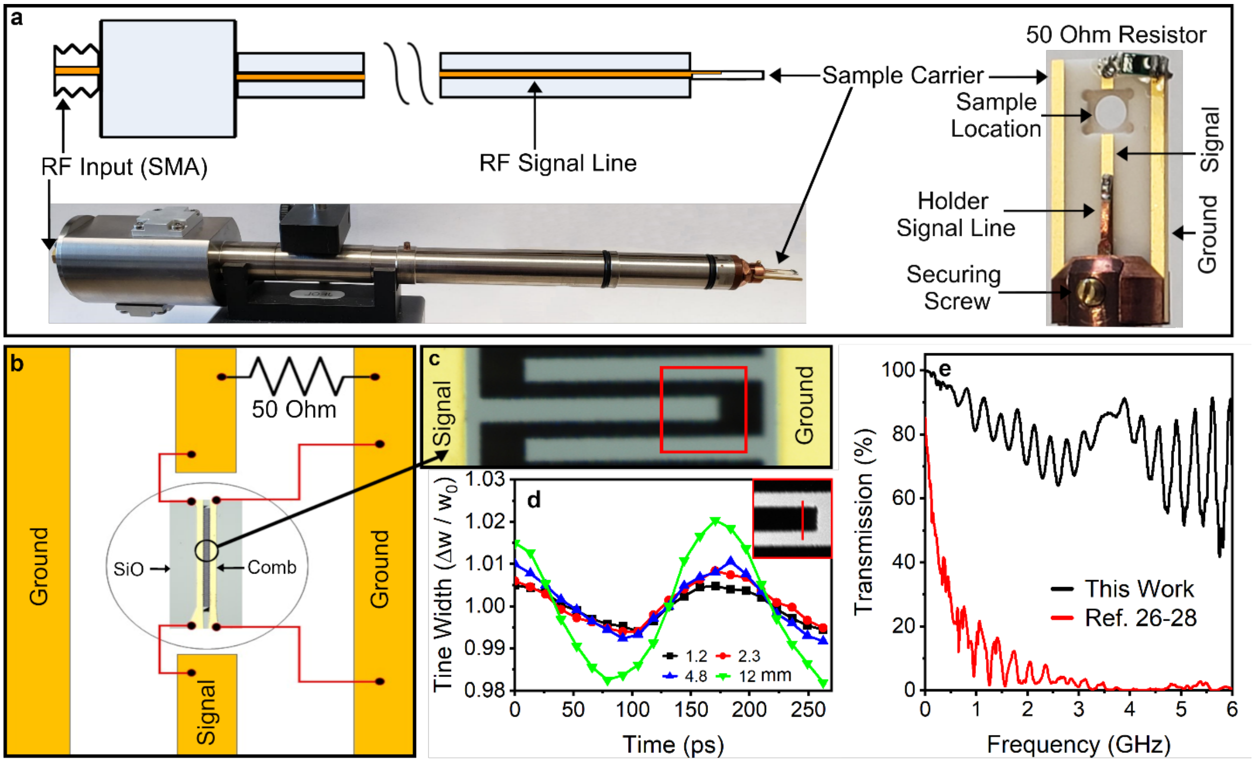

Figure 6. Development of a low-loss stroboscopic TEM holder for RF excitation. (a) Schematic and image of the RF compatible holder using a PCB chip carrier as the sample mounting substrate. A thorough description of the holder is available in the supplementary information. (b) Electrical connections between the carrier PCB and interdigitated silicon comb structure used for time-resolved evaluation. Red lines represent wire bonding between the PCB and ≈3 mm sample structure. The 50 Ω resistor is designed to match the impedance between the sample and PCB. (c) Optical microscopy image of the interdigitated silicon comb using a reflection geometry. (d) Time-resolved tine width measurement (along red line in inset) of the interdigitated comb sample

using an excitation power of ≈0.5 W and four defocus heights (≈1.2 mm, ≈2.3 mm, ≈4.8 mm, ≈12 mm). (e) Power transmission measurements for the new RF compatible TEM holder compared to previous publications [26,27].

Through the imaging capabilities of the pulser we have further pushed our capabilities to conduct laser-free UEM experiments at high spatiotemporal resolutions. Specifically, our new RF compatible TEM holder enables substantial improvement in RF signal transmission over a (0 to6) GHz frequency range [26,27]. Diverging from focus also disperses the range of momentum vectors in the electron beam at the image plane causing the apparent tine width fluctuation to amplify during peaks and valleys in RF excitation. The result is like other defocusing techniques that amplify contrast mechanisms (*i.e.,* Lorentz imaging) where larger defocus values cause a larger dispersion of the electron momenta during the beam-specimen interaction (see Fig. 6d). The apparent deflection of the electrons becomes stronger causing the effective size fluctuation of the tines to increase. Observed breathing modes due to the electrostatic deflection can potentially be utilized to study other indirect dynamics such as spin-wave generation or propagation in spintronic devices. We expect that our advancements on the electron pulser will push the boundary of time-resolved dynamic elucidation to each of the techniques which have presented throughout this discussion.

4. SUMMARY AND CONCLUSIONS

In summary, we have demonstrated enhanced imaging capabilities using the electron pulser in a traditional TEM with a newly installed high-resolution polepiece at BNL to illustrate its performance in various microscopy techniques. Each technique utilizing a pulsed electron beam was compared to the continuous mode. In every technique, electron counts decrease by nearly 80 %, even though physical measurements such as lattice spacings and spin contrast are retained. As a result, the immediate negative consequence for the user is longer acquisition times (inversely proportional to beam duty cycle) than a traditional microscope. Furthermore, the best results are yielded for the non-ultrahigh magnification techniques, as the influence of RF field sweeping is less noticeable. Clearly, the development of the electron pulser is still in its infancy and there are still improvements which can be made, but the current performance can capture structural features as small as 0.2 nm. Further, the electron beam coherency is retained better for features aligned parallel to the sweeping direction of the RF field. We have also built a new RF compatible TEM holder which can transmit over 40 % more power to the sample during excitation which will enable more efficient probing of electronic, magnetic and structural dynamics.

ASSOCIATED CONTENT

Supporting Information

The Supporting Information includes additional details about the Materials and Methods, six Supplementary Figures of the procedures and explanations and one supplementary table of modulation and demodulation parameters.

Author Information

Corresponding Author

*Email: zhu@bnl.gov

ORCID

Yimei Zhu: 0000-0002-1638-7217

Spencer A. Reisbick: 0000-0002-7882-4152

M-G Han:

Chuhang Liu: 0000-0001-7162-4708

Eric Montgomery:

Chunguang Jing: 0000-0002-3333-1231

Yubin Zhao: 0000-0003-2327-8921

June W. Lau: 0000-0002-5233-4956

Jason J. Gorman: 0000-0003-2148-2312

Funding

This work was partially supported by the Materials Science and Engineering Divisions, Office of Basic Energy Sciences of the U.S. Department of Energy under Contract No. DESC0012704. The electron pulser was developed by Euclid through the DOE's SBIR grant under contract DE-SC0013121.

Notes

The authors declare no competing financial interest.

Acknowledgements

We thank JEOL engineers Robert Connor and Joseph Girgis for their time during installation week to optimize the emission parameters and alignment of the microscope.

REFERENCES

[1] P.E. Batson, N. Dellby, O.L. Krivanek, Sub-ångstrom resolution using aberration corrected electron optics, Nature. 418 (2002) 617–620. https://doi.org/10.1038/nature00972.

[2] R. Erni, M.D. Rossell, C. Kisielowski, U. Dahmen, Atomic-resolution imaging with a sub-50-pm electron probe, Phys. Rev. Lett. 102 (2009) 1–4. https://doi.org/10.1103/PhysRevLett.102.096101.

[3] A.R. Faruqi, Direct Electron Detectors for Electron Microscopy, Adv. Imaging Electron Phys. 145 (2007) 55–93. https://doi.org/10.1016/S1076-5670(06)45002-3.

[4] A.R. Faruqi, D.M. Cattermole, C. Raeburn, Direct electron detection methods in electron microscopy, Nucl. Instruments Methods Phys. Res. Sect. A Accel. Spectrometers, Detect. Assoc. Equip. 513 (2003) 317–321. https://doi.org/10.1016/j.nima.2003.08.055.

[5] T. Komoda, Study on the Structure of Evaporated Gold Particles by Means of a High Resolution Electron Microscope, Jpn. J. Appl. Phys. 7 (1968) 27–30. https://doi.org/10.1143/jjap.7.27.

[6] J.I. Goldstein, C.E. Lyman, D.B. Williams, The wavelength-dispersive spectrometer and its proposed use in the Analytical Electron Microscope, Ultramicroscopy. 28 (1989) 162–164. https://doi.org/10.1016/0304-3991(89)90289-1.

[7] L.A. Bendersky, F.W. Gayle, Electron Diffraction Using Transmission Electron Microscopy, J. Res. Natl. Inst. Stand. Technol. 106 (2001) 997–1012. https://doi.org/10.6028/jres.106.051.

[8] D.B. Williams, C.B. Carter, Transmission Electron Microscopy, 2nd ed., Springer Science, New York, 1996.

[9] A.R. Faruqi, G. McMullan, Direct imaging detectors for electron microscopy, Nucl.

Instruments Methods Phys. Res. Sect. A Accel. Spectrometers, Detect. Assoc. Equip. 878 (2018) 180–190. https://doi.org/10.1016/j.nima.2017.07.037.

[10] C.M. O'Leary, C.S. Allen, C. Huang, J.S. Kim, E. Liberti, P.D. Nellist, A.I. Kirkland, Phase reconstruction using fast binary 4D STEM data, Appl. Phys. Lett. 116 (2020) 124101. https://doi.org/10.1063/1.5143213.

[11] I. MacLaren, T.A. MacGregor, C.S. Allen, A.I. Kirkland, Detectors-The ongoing revolution in scanning transmission electron microscopy and why this important to material characterization, APL Mater. 8 (2020) 110901. https://doi.org/10.1063/5.0026992.

[12] E.J. Vandenbussche, D.J. Flannigan, Reducing Radiation Damage in Soft Matter with Femtosecond-Timed Single-Electron Packets, Nano Lett. 19 (2019) 6687–6694. https://doi.org/10.1021/acs.nanolett.9b03074.

[13] R.M. Glaeser, K.A. Taylor, Radiation damage relative to transmission electron microscopy of biological specimens at low temperature: a review, J. Microsc. 112 (1978) 127–138. https://doi.org/10.1111/j.1365-2818.1978.tb01160.x.

[14] T. Wang, W. Lu, Q. Yang, S. Li, X. Yu, J. Qiu, X. Xu, S.F. Yu, In Situ Observation of Nucleation and Crystallization of a Single Nanoparticle in Transparent Media, J. Phys. Chem. C. 124 (2020) 15533–15540. https://doi.org/10.1021/acs.jpcc.0c03402.

[15] I. Akimoto, Y. Handa, K. Fukai, N. Naka, High carrier mobility in ultrapure diamond measured by time-resolved cyclotron resonance, Appl. Phys. Lett. 105 (2014) 032102. https://doi.org/10.1063/1.4891039.

[16] U. Bovensiepen, P.S. Kirchmann, Elementary relaxation processes investigated by femtosecond photoelectron spectroscopy of two-dimensional materials, Laser Photonics Rev. 6 (2012) 589–606. https://doi.org/10.1002/lpor.201000035.

[17] F.U. Stein, L. Bocklage, M. Weigand, G. Meier, Time-resolved imaging of nonlinear magnetic domain-wall dynamics in ferromagnetic nanowires, Sci. Rep. 3 (2013) 7–10. https://doi.org/10.1038/srep01737.

[18] J. Vogel, W. Kuch, M. Bonfim, J. Camarero, Y. Pennec, F. Offi, K. Fukumoto, J. Kirschner, A. Fontaine, S. Pizzini, Time-resolved magnetic domain imaging by x-ray photoemission electron microscopy, Appl. Phys. Lett. 82 (2003) 2299–2301. https://doi.org/10.1063/1.1564876.

[19] Z. Chen, K.J. Satzinger, J. Atalaya, A.N. Korotkov, A. Dunsworth, D. Sank, C. Quintana, M. McEwen, R. Barends, P. V. Klimov, S. Hong, C. Jones, A. Petukhov, D. Kafri, S. Demura, B. Burkett, C. Gidney, A.G. Fowler, A. Paler, H. Putterman, I. Aleiner, F. Arute, K. Arya, R. Babbush, J.C. Bardin, A. Bengtsson, A. Bourassa, M. Broughton, B.B. Buckley, D.A. Buell, N. Bushnell, B. Chiaro, R. Collins, W. Courtney, A.R. Derk, D. Eppens, C. Erickson, E. Farhi, B. Foxen, M. Giustina, A. Greene, J.A. Gross, M.P. Harrigan, S.D. Harrington, J. Hilton, A. Ho, T. Huang, W.J. Huggins, L.B. Ioffe, S. V. Isakov, E. Jeffrey, Z. Jiang, K. Kechedzhi, S. Kim, A. Kitaev, F. Kostritsa, D. Landhuis, P. Laptev, E. Lucero, O. Martin, J.R. McClean, T. McCourt, X. Mi, K.C. Miao, M. Mohseni, S. Montazeri, W. Mruczkiewicz, J. Mutus, O. Naaman, M. Neeley, C. Neill, M. Newman, M.Y. Niu, T.E. O'Brien, A. Opremcak, E. Ostby, B. Pató, N. Redd, P. Roushan, N.C. Rubin, V. Shvarts, D. Strain, M. Szalay, M.D. Trevithick, B. Villalonga, T. White, Z.J. Yao, P. Yeh, J. Yoo, A. Zalcman, H. Neven, S. Boixo, V. Smelyanskiy, Y. Chen, A. Megrant, J. Kelly, Exponential suppression of bit or phase errors with cyclic error correction, Nature. 595 (2021) 383–387. https://doi.org/10.1038/s41586-021-03588-y.

[20] N.M. Linke, D. Maslov, M. Roetteler, S. Debnath, C. Figgatt, K.A. Landsman, K. Wright,

C. Monroe, Experimental comparison of two quantum computing architectures, Proc. Natl. Acad. Sci. U. S. A. 114 (2017) 3305–3310. https://doi.org/10.1073/pnas.1618020114.

[21] T. Schneider, A.A. Serga, B. Leven, B. Hillebrands, R.L. Stamps, M.P. Kostylev, Realization of spin-wave logic gates, Appl. Phys. Lett. 92 (2008) 022505. https://doi.org/10.1063/1.2834714.

[22] Y. Kajiwara, K. Harii, S. Takahashi, J. Ohe, K. Uchida, M. Mizuguchi, H. Umezawa, H. Kawai, K. Ando, K. Takanashi, S. Maekawa, E. Saitoh, Transmission of electrical signals by spin-wave interconversion in a magnetic insulator, Nature. 464 (2010) 262–266. https://doi.org/10.1038/nature08876.

[23] A. Feist, N. Bach, N. Rubiano da Silva, T. Danz, M. Möller, K.E. Priebe, T. Domröse, J.G. Gatzmann, S. Rost, J. Schauss, S. Strauch, R. Bormann, M. Sivis, S. Schäfer, C. Ropers, Ultrafast transmission electron microscopy using a laser-driven field emitter: Femtosecond resolution with a high coherence electron beam, Ultramicroscopy. 176 (2017) 63–73. https://doi.org/10.1016/j.ultramic.2016.12.005.

[24] D.A. Plemmons, D.J. Flannigan, Ultrafast electron microscopy: Instrument response from the single-electron to high bunch-charge regimes, Chem. Phys. Lett. 683 (2017) 186–192. https://doi.org/10.1016/j.cplett.2017.01.055.

[25] L. Zhang, J.P. Hoogenboom, B. Cook, P. Kruit, Photoemission sources and beam blankers for ultrafast electron microscopy, Struct. Dyn. 6 (2019) 051501. https://doi.org/10.1063/1.5117058.

[26] J.W. Lau, K.B. Schliep, M.B. Katz, V.J. Gokhale, J.J. Gorman, C. Jing, A. Liu, Y. Zhao, E. Montgomery, H. Choe, W. Rush, A. Kanareykin, X. Fu, Y. Zhu, Laser-free GHz stroboscopic transmission electron microscope: Components, system integration, and

practical considerations for pump-probe measurements, Rev. Sci. Instrum. 91 (2020) 021301. https://doi.org/10.1063/1.5131758.

[27] X. Fu, E. Wang, Y. Zhao, A. Liu, E. Montgomery, V.J. Gokhale, J.J. Gorman, C. Jing, J.W. Lau, Y. Zhu, Direct visualization of electromagnetic wave dynamics by laser-free ultrafast electron microscopy, Sci. Adv. 6 (2020) eabc3456. https://doi.org/10.1126/sciadv.abc3456.

[28] C. Jing, Y. Zhu, A. Liu, K. Schliep, X. Fu, Y. Zhao, E. Montgomery, W. Rush, A. Kanareykin, M. Katz, J. Lau, Tunable electron beam pulser for picoseconds stroboscopic microscopy in transmission electron microscopes, Ultramicroscopy. 207 (2019) 112829. https://doi.org/10.1016/j.ultramic.2019.112829.

[29] R.W. Vook, M.A. Otooni, Lattice parameter of thin gold films, J. Appl. Phys. 39 (1968) 2471–2472. https://doi.org/10.1063/1.1656581.

[30] A. Gentils, J.N. Chapman, G. Xiong, R.P. Cowburn, Variation of domain-wall structures and magnetization ripple spectra in permalloy films with controlled uniaxial anisotropy, J. Appl. Phys. 98 (2005) 053905. https://doi.org/10.1063/1.2033152.

[31] M. De Graef, Recent advances in quantitative Lorentz microscopy, INTERMAG Eur. 2002 - IEEE Int. Magn. Conf. (2002) 1–22. https://doi.org/10.1109/INTMAG.2002.1001118.

[32] V. V. Volkov, Y. Zhu, Lorentz phase microscopy of magnetic materials, Ultramicroscopy. 98 (2004) 271–281. https://doi.org/10.1016/j.ultramic.2003.08.026.

[33] C. Liu, J. Chen, T. Liu, F. Heimbach, H. Yu, Y. Xiao, J. Hu, M. Liu, H. Chang, T. Stueckler, S. Tu, Y. Zhang, Y. Zhang, P. Gao, Z. Liao, D. Yu, K. Xia, N. Lei, W. Zhao, M. Wu, Long-distance propagation of short-wavelength spin waves, Nat. Commun. 9 (2018) 4–11. https://doi.org/10.1038/s41467-018-03199-8.

[34] S.A. Reisbick, Y. Zhang, D.J. Flannigan, Influence of Discrete Defects on Observed

Acoustic-Phonon Dynamics in Layered Materials Probed with Ultrafast Electron Microscopy, J. Phys. Chem. A. 124 (2020) 1877–1884. https://doi.org/10.1021/acs.jpca.9b12026.

[35] D.X. Du, D.J. Flannigan, Imaging phonon dynamics with ultrafast electron microscopy: Kinematical and dynamical simulations, Struct. Dyn. 7 (2020) 024103. https://doi.org/10.1063/1.5144682.

[36] A. Feist, N. Rubiano Da Silva, W. Liang, C. Ropers, S. Schäfer, Nanoscale diffractive probing of strain dynamics in ultrafast transmission electron microscopy, Struct. Dyn. 5 (2018) 014302. https://doi.org/10.1063/1.5009822.

[37] D.R. Cremons, D.X. Du, D.J. Flannigan, Picosecond phase-velocity dispersion of hypersonic phonons imaged with ultrafast electron microscopy, Phys. Rev. Mater. 1 (2017) 073801. https://doi.org/10.1103/PhysRevMaterials.1.073801.

[38] A.J. McKenna, J.K. Eliason, D.J. Flannigan, Spatiotemporal Evolution of Coherent Elastic Strain Waves in a Single MoS2 Flake, Nano Lett. 17 (2017) 3952–3958. https://doi.org/10.1021/acs.nanolett.7b01565.

[39] D.R. Cremons, D.A. Plemmons, D.J. Flannigan, Defect-mediated phonon dynamics in TaS2 and WSe2, Struct. Dyn. 4 (2017) 044019. https://doi.org/10.1063/1.4982817.

[40] D.R. Cremons, D.A. Plemmons, D.J. Flannigan, Femtosecond electron imaging of defect-modulated phonon dynamics, Nat. Commun. 7 (2016) 11230. https://doi.org/10.1038/ncomms11230.

[41] A. Yurtsever, A.H. Zewail, Kikuchi ultrafast nanodiffraction in four-dimensional electron microscopy, Proc. Natl. Acad. Sci. U. S. A. 108 (2011) 3152–3156. https://doi.org/10.1073/pnas.1018733108.

[42] O.H. Kwon, B. Barwick, H.S. Park, J.S. Baskin, A.H. Zewail, Nanoscale mechanical drumming visualized by 4D electron microscopy, Nano Lett. 8 (2008) 3557–3562. https://doi.org/10.1021/nl8029866.

[43] J.W. Lau, M. Beleggia, Y. Zhu, Common reversal mechanisms and correlation between transient domain states and field sweep rate in patterned Permalloy structures, J. Appl. Phys. 102 (2007) 1–6. https://doi.org/10.1063/1.2769779.

[44] J.W. Lau, M. Beleggia, M.A. Schofield, G.F. Neumark, Y. Zhu, Direct correlation of reversal rate dynamics to domain configurations in micron-sized permalloy elements, J. Appl. Phys. 97 (2005) 22–24. https://doi.org/10.1063/1.1851731.

[45] T.E. Gureyev, A. Roberts, K.A. Nugent, Partially coherent fields, the transport-of-intensity equation, and phase uniqueness, J. Opt. Soc. Am. A. 12 (1995) 1942. https://doi.org/10.1364/josaa.12.001942.

[46] M. Beleggia, M.A. Schofield, V. V. Volkov, Y. Zhu, On the transport of intensity technique for phase retrieval, Ultramicroscopy. 102 (2004) 37–49. https://doi.org/10.1016/j.ultramic.2004.08.004.

[47] A. Kohn, A. Habibi, M. Mayo, Experimental evaluation of the “transport-of-intensity” equation for magnetic phase reconstruction in Lorentz transmission electron microscopy, Ultramicroscopy. 160 (2016) 44–56. https://doi.org/10.1016/j.ultramic.2015.09.011.

[48] P.K. Olshin, G. Bongiovanni, M. Drabbels, U.J. Lorenz, Atomic-Resolution Imaging of Fast Nanoscale Dynamics with Bright Microsecond Electron Pulses, Nano Lett. 21 (2021) 612–618. https://doi.org/10.1021/acs.nanolett.0c04184.

[49] F. Houdellier, A. Masseboeuf, M. Monthioux, M.J. Hÿtch, New carbon cone nanotip for use in a highly coherent cold field emission electron microscope, Carbon N. Y. 50 (2012)

2037–2044. https://doi.org/10.1016/j.carbon.2012.01.023.

[50] M.R. Scheinfein, W. Qian, J.C.H. Spence, Aberrations of emission cathodes: Nanometer diameter field-emission electron sources, J. Appl. Phys. 73 (1993) 2057–2068. https://doi.org/10.1063/1.353151.

[51] J.C.H. Spence, W. Qian, M.P. Silverman, Electron source brightness and degeneracy from Fresnel fringes in field emission point projection microscopy, J. Vac. Sci. Technol. A Vacuum, Surfaces, Film. 12 (1994) 542–547. https://doi.org/10.1116/1.579166.

Supporting Information for

Stroboscopic Imaging Capabilities Using RF Strip-lines in a Commercial Electron Microscope

Spencer A. Reisbick[1], Myung-Geun Han[1], Chuhang Liu[1,3], Yubin Zhao[2], Eric Montgomery[2], Vikrant J. Gokhale[4], Jason J. Gorman[4], Chunguang Jing[2], June W. Lau[5] and Yimei Zhu[1,*]

[1]*Condensed Matter Physics and Materials Science Department, Brookhaven National Laboratory, Upton, NY 11973, USA*
[2]*Euclid Techlabs LLC, 365 Remington Blvd. Bolingbrook, IL 60440, USA*
[3]*Department of Physics and Astronomy, Stony Brook University, Stony Brook, NY 11794, USA*
[4]*Microsystems and Nanotechnology Division, National Institute of Standards and Technology, Gaithersburg, MD 20899, USA.*
[5]*Materials Science and Engineering Division, National Institute of Standards and Technology, Gaithersburg, MD 20899, USA.*

*Author to whom correspondence should be addressed.
Email: zhu@bnl.gov
Office: 631-344-3057

The Supporting Information includes:

Materials and Methods
Figures S1-S6
Table S1
Equations S1-S3

Materials and Methods

Electron beam measurements using the electron pulser

The diameter and sharpness of the electron beam were measured during pulsed and continuous operation by expanding the beam until it was approximately 90 % the size of the camera. Due to camera limitations, only certain magnifications were used in continuous mode to prevent saturation. As a result, images using a pulsed beam were acquired directly after the conditions for the continuous beam. Figure S1 contains the micrograph of the pulsed electron beam where the red line dictates the location of the beam profiles in (b)-(d). The pulsed and continuous beams share similar beam profiles, but the pulsed beam is because so many electrons are dumped (Figures S1b and S1c). A 10 μm aperture was used to reduce the intensity as low as possible. Figure S1d contains one edge of the line profile and the corresponding error function fit using equation S1.

$$y = A * \mathrm{erf}\left(\frac{x - x_0}{\sigma}\right) \tag{S1}$$

Here, A is the amplitude, x_0 is the lateral displacement and σ is the FWHM, or the blur parameter in the main text. Figures 1e and 1f show the measured beam currents at the base of the microscope before and after pulser installation for different magnification modes. Multiple trials were acquired for each as represented by the error bars in the main text.

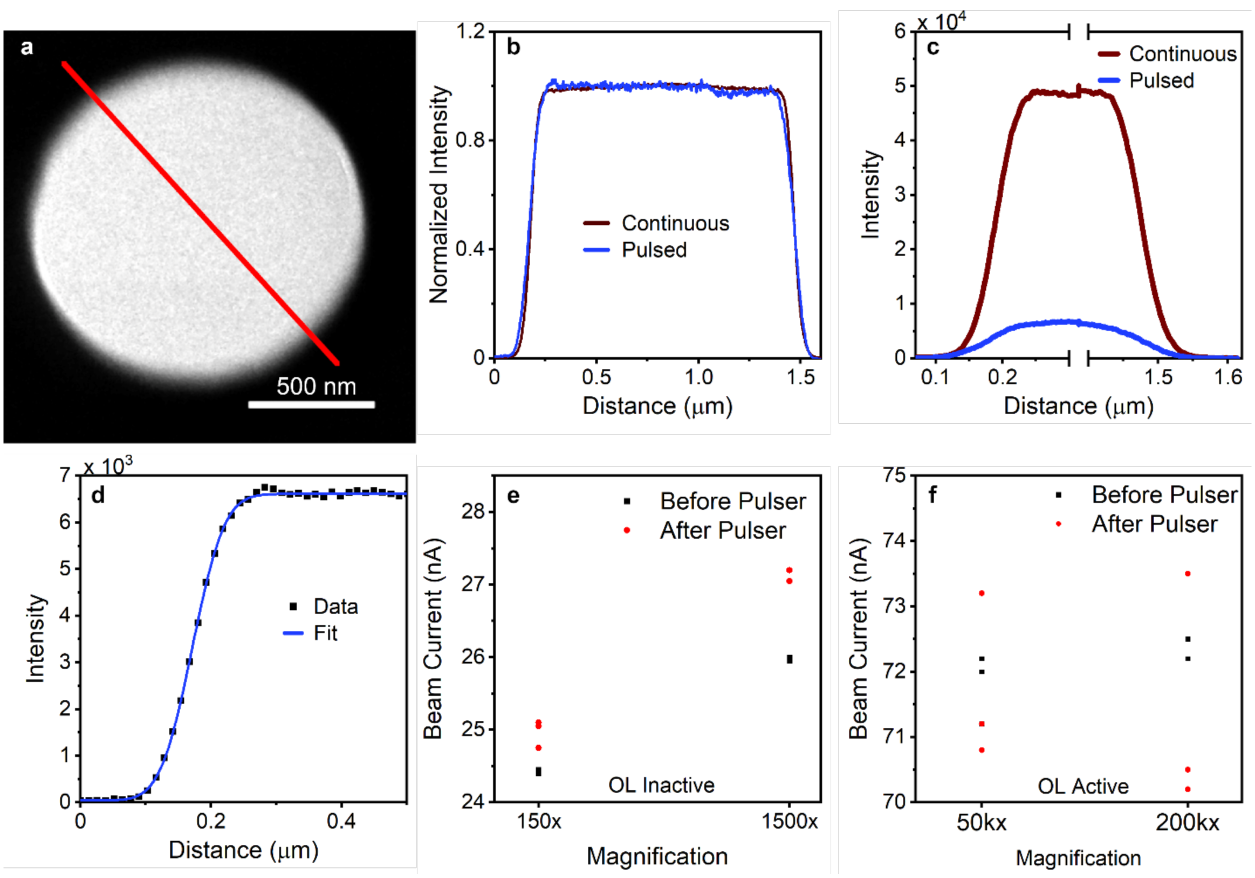

Figure S1. Characterization of the pulsed electron beam. (a) Image of the pulsed electron beam with a 10 µm condenser aperture. The red line corresponds to the position of the line profiles provided in (b)-(d). (b) Normalized comparison of the shape of the continuous (maroon) and pulsed (blue) electron beams. (c) Absolute intensity difference between continuous and pulsed electron beams. (d) Line profile of a portion of the pulsed electron beam fit to an error function. The fit parameters were used to create the quantitative comparisons presented in Figure 1. (e, f) Maximum achievable beam current measurements before and after installation of the electron pulser in magnification mode (e) and low magnification mode (f). Measurements are made over three different days before and after installation to check the stability of the installation.

Quantitative measurements for bright field and diffraction images

Bright field imaging and diffraction were quantitatively compared using line profiles across contrast boundaries. Figure S2a contains the bright field image used in the main text and Figure S2b is a magnified version. The image has some intentional astigmatism to enhance the contrast at the edge of the latex spheres. The difference in positions between the 90^{th} and 10^{th} percentiles of the intensity across the sphere edge corresponds to the sharpness in Figure 2 [1]. In diffraction (Figures S2d-S2f), the center was identified using a circular Hough transform due to the placement of the beam block. From this position, the intensity was radially integrated outward from the pattern center. Radial peaks corresponding to the 111 and 200 planes were fit to Equation S2.

$$y = B * e^{\left(-\frac{x-x_1}{\sigma_1}\right)} + C * e^{\left(-\frac{(x-x_2)^2}{\sigma_2}\right)} + D * e^{\left(-\frac{(x-x_3)^2}{\sigma_3}\right)} \quad \text{(S2)}$$

The fitting parameter includes an exponential decay and two Gaussians for the background and diffraction rings respectively. Each resulting fit parameters was used to create the quantitative comparisons in Figure 2.

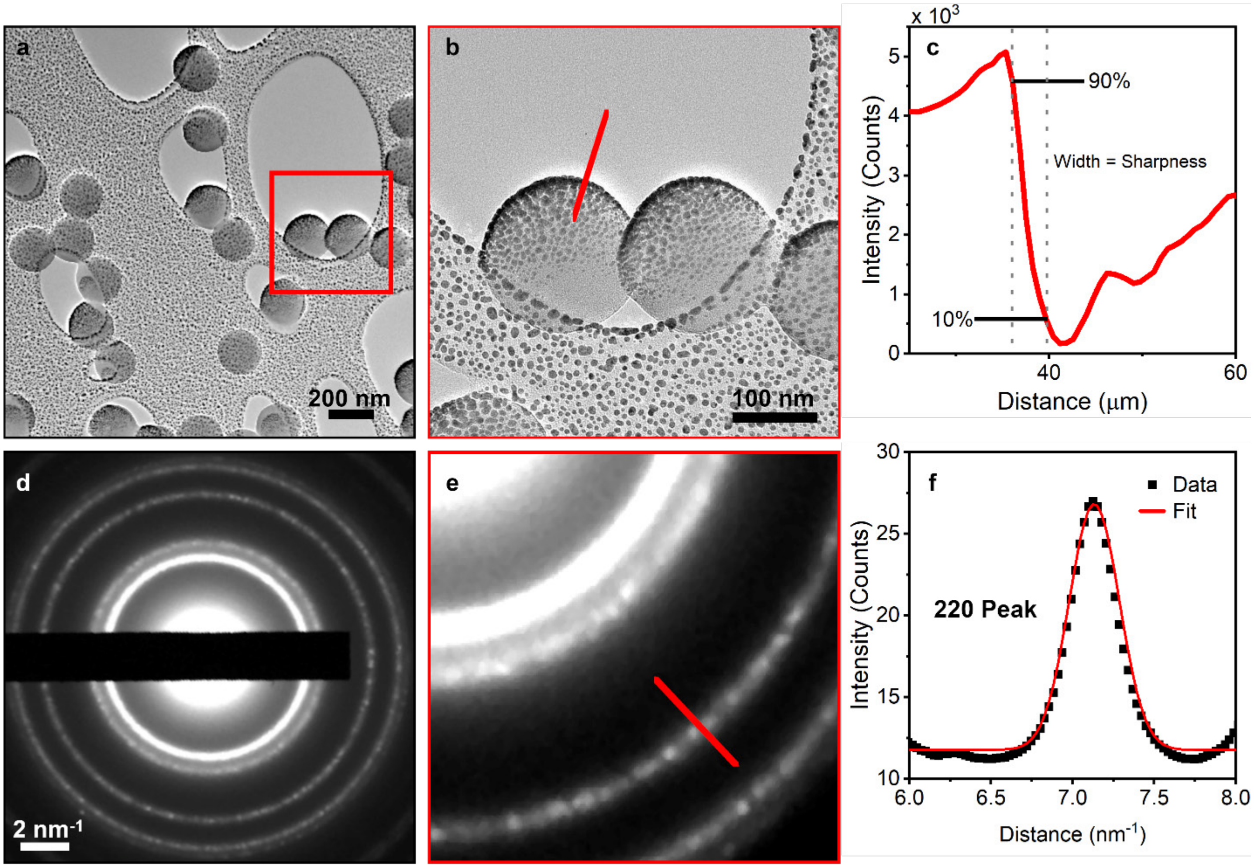

Figure S2. Techniques used to develop quantitative comparisons between bright field imaging and diffraction. (a) Bright field image of latex spheres and gold nanoparticles on holey carbon using a continuous beam. (b) Magnified image of latex spheres from the red box in (a). The red line corresponds to one example of the line profile used to make quantitative measurements. (c) Line profile along the edge of a latex sphere with the difference between the 90 % and 1 0% positions defining the width. Error bars in the main text are the standard deviation of the profiles for five different spheres. (d) Diffraction pattern of gold nanoparticles using a continuous electron beam. (e) Magnified image of one portion of the 111 and 200 rings from the red box in (d). (f) Line profile from radially averaged profile of the diffraction pattern. The fit corresponds to the sum of a background exponential decay and two Gaussians.

Quantitative comparison of Py vortex centers during LTEM

We have presented the first demonstration of spin reconstruction using a pulsed electron beam. Here, we include a quantitative comparison of the vortex core when fit to a single Gaussian function defined by Equation S3.

$$y = A_{vor} * \exp\left(-\frac{(x-x_0)^2}{\sigma_0}\right) + b \qquad \text{(S3)}$$

Here, A_{vor} is the amplitude, x_0 is the position of the vortex center, σ_o is related to the FWHM and b is the background. The intensity ratio in Figure 3 of the main text is A_{vor}/b. Figure S3 contains the continuous and pulsed images present in the main text along with the fit parameters. Noticeably, the intensity measurements (amplitude and baseline) retain the 80 % reductions, like the other imaging modalities. However, the intensity ratio (amplitude/baseline) remains within statistical similarity to one another. As well, the width of the vortex core is retained during pulsed beam imaging.

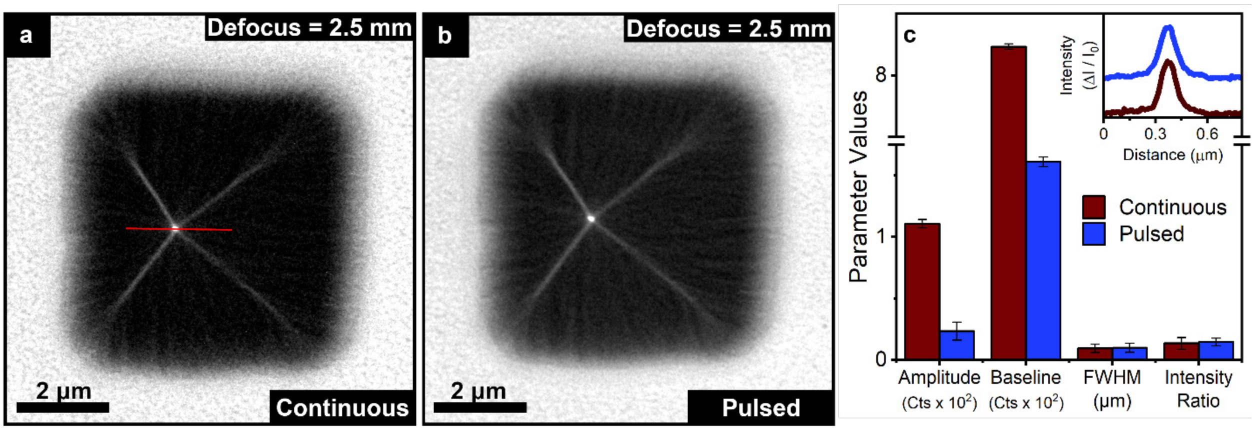

Figure S3. Quantitative comparison of the magnetic vortex cores using a pulsed and continuous electron beam. (a, b) Continuous (a) and pulsed (b) images of a Py square at a defocus of 2.5 mm showing the vortex core and magnetic ripple contrast. (c) Fit parameters for a single Gaussian function along the red line in (a) with each line profile in the inset. The intensity ratio is the amplitude divided by the baseline and FWHM is the width of the peak.

Control experiments and extraction of time-resolved dynamics in an interdigitated silicon comb using UEM

Since UEM experiments are stroboscopic, control experiments are necessary to verify that the emerging dynamics are not because of long-term sample motion. In Figure S4, we present essential measurements in the UEM setup as verification of the time-resolved dynamics we observe. Figures S4b contains the tine width extraction by fitting each edge to an error function (Equation S1) and taking the difference of the positions. Figure S4c contains the amplitude of the breathing modes for the tines with respect to defocus. Figures S4d-S4f are each control experiments used to verify the results presented in the main text. Figures S4d utilizes a technique known as time-point randomization. During acquisition, the images are collected in a random sequence (*i.e.* 10 ps, 50 ps, 100 ps, 30 ps, 80 ps, etc.). The red curve shows the order of image collection and the black curve is the unscrambled temporal positions. If the data does not contain artifacts, the acquisition order sequence should be incoherent, with a coherent time-order sequence. Figure S4e contains another control checking that modifying the excitation frequency of our continuous RF cycle results in a matching frequency shift. Note that for pulsed pumping techniques, the sample response frequency would not be equal to the excitation frequency, but here we utilize a phase perturbation [2].

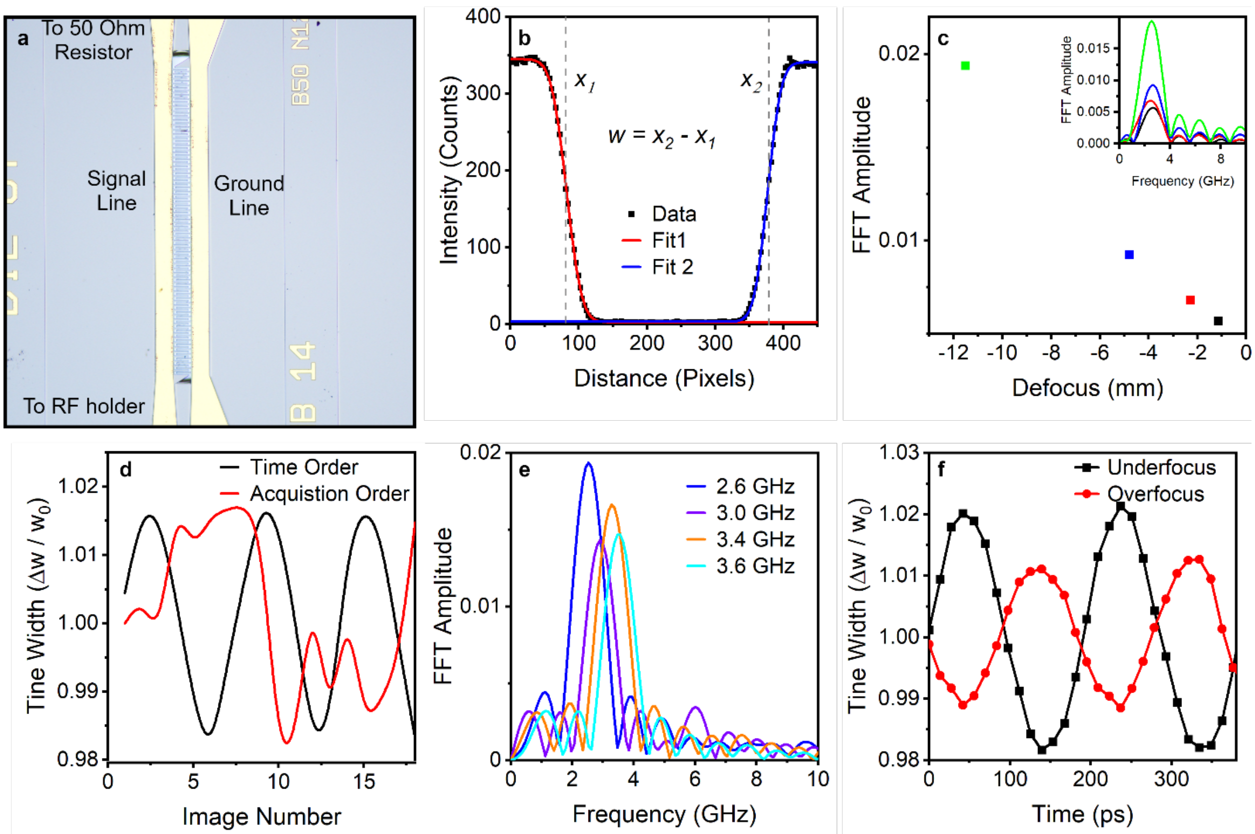

Figure S4. Extraction and verification of time-resolved electrostatic breathing modes in an interdigitated comb. (a) Optical microscopy image of the interdigitated silicon comb with the signal and ground line indicated. (b) Line profile along a tine of the interdigitated comb with two error function fits (Equation S1) at each edge. The difference of the positions is the tine width. (c) Electrostatic deflection magnitudes for different electron beam defocus. The inset is the FFT of each intensity profile. (d) Randomized image acquisition to act as a control for stroboscopic imaging. (e) Control experiment used to identify the proper excitation frequency of the interdigitated comb. An identical experiment was conducted at each excitation frequency to verify that the extracted dynamics match the phase dependent excitation. (f) Comparison between under and over focusing the electron beam which phase shifts the dynamics by pi.

Progression of pulser operation used for coherent image acquisition.

Figure S5 contains the procedure to demodulate the electron beam using 2000 mesh evaporated Py squares on silicon nitride. The squares form a magnetic vortex or seven-domain state when imaged using Lorentz phase TEM. The microscope starts in normal operation (Figure S7a). When the power to the amplifiers controlling K1 and K2 is activated, the beam blurs slightly, but this is only visible at high magnifications (Figure S5b). The K1 voltage is the first strip-line activated, resulting in severe blurriness in the image (Figure S7c). However, it is compensated by K2 with a demodulating voltage that is 180° out-of-phase from K1. Next, the chopping aperture is inserted causing an 80 % reduction in intensity but improving the quality of the image (Figure S5f). We have added Figure S5e to demonstrate the quality when K2 is deactivated, and the chopping aperture is inserted. Notably, the quality of the image is ok, meaning that the sweeping motion of K1 has the strongest distortion in image creation.

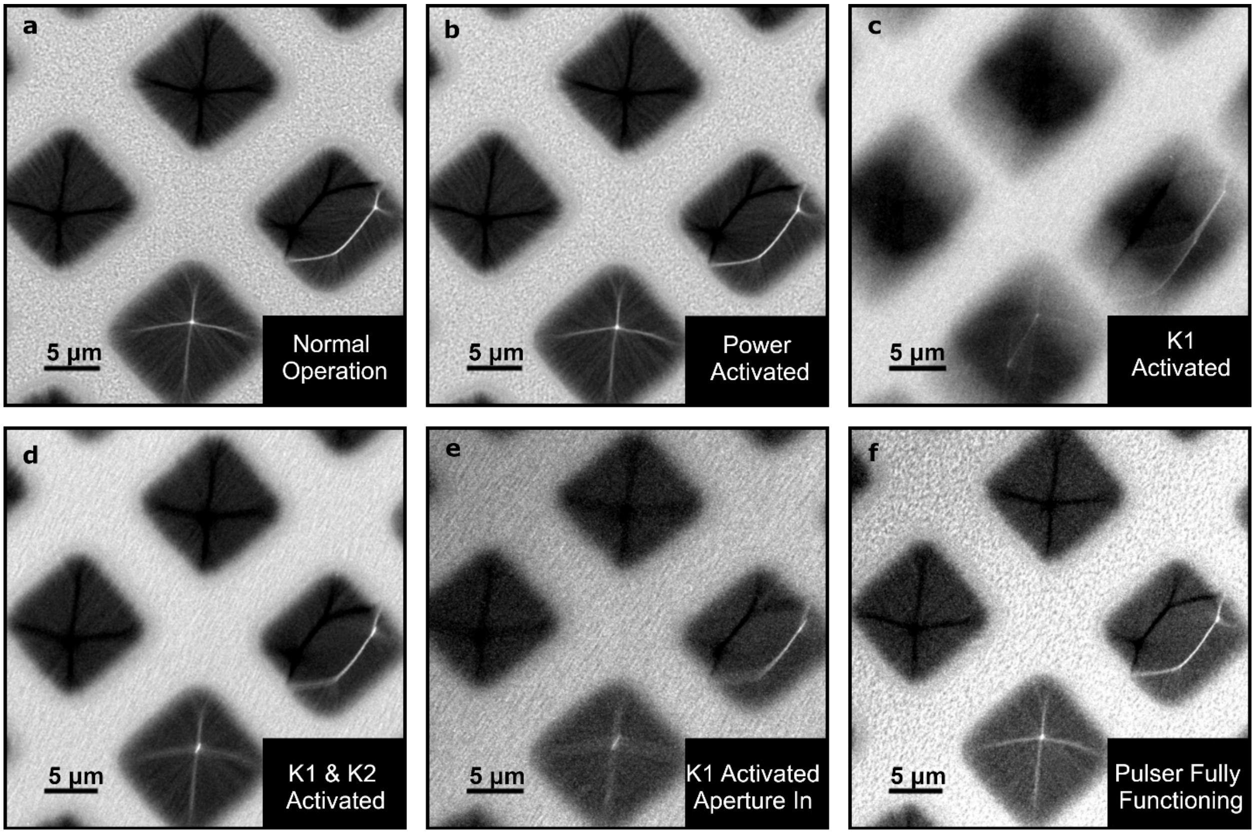

Figure S5. Graphical operation procedure of the electron pulser using 2000 mesh Py squares. (a) Operation of traditional TEM with the pulser inserted, but all electronics are unpowered. (b) The power to the pulser is activated, but both K1 and K2 are set to voltages of zero. (c) Image acquired when the K1 voltage is set to 0.3 V. (d) Appearance of the Py sample when K2 is used to demodulate the electron beam (See Table S1 for pulser parameters). (e) Image quality when K1 is modulating the beam through a 25 µm chopping aperture, but K2 is not active. (f) Final pulsed beam image where K1 = 0.3 V, K2 = 0.05 V and $\varphi = 24°$.

Description of the newly developed RF compatible TEM holder for UEM experiments

Previously, over 50 % of the RF power designed for excitation was lost before reaching the sample, so a new holder was designed to improve the transmission rates [2]. The newly developed holder has a signal line running down the center of the holder and exits near the opposite end as shown in Figure S8. A custom PCB has been developed as an interchangeable component for this RF holder because most electrical connections to the samples are permanent. We utilize a screw to secure the PCB to the holder causing contact between the signal lines of the holder and PCB.

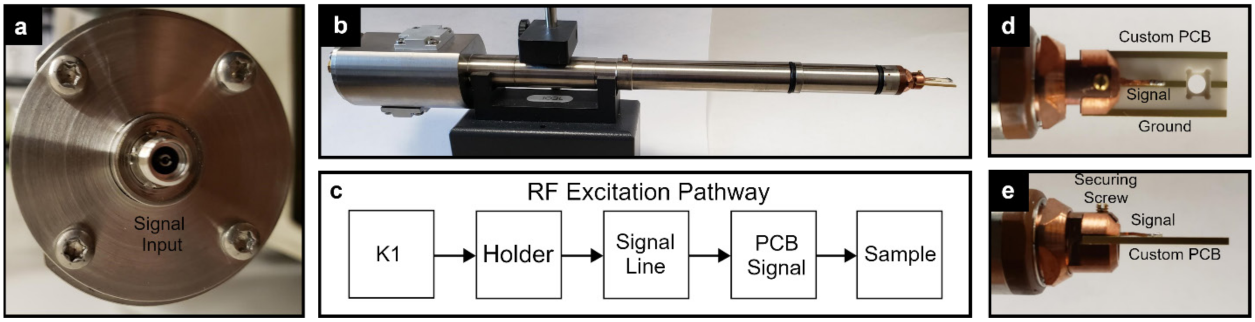

Figure S6. Newly developed RF compatible TEM holder. (a) Rear of the holder with a RF signal input connected *via* SMA connection. (b) Side view of the newly developed holder with the compatible PCB inserted. (c) Excitation pathway for RF from K1 to the sample. Depending on the sample, wire bonding or soldering can be used to secure the sample into the PCB and make the necessary electrical connections. (d, e) Top (d) and side (e) views of the custom PCB for sample mounting in the RF holder. The center gold strip is the signal line and the edges are ground. A securing screw is tightened to lock the PCB in place and create the contact.

Pulser operating parameters during image acquisition during pulsed beam operation

Demodulation parameters in K2 are dependent on the RF frequency, K1 voltage and microscope alignments. Table S1 includes pulsed beam parameters for each of the techniques described throughout the text. The K1 and K2 voltages are applied across each RF strip-line and the phase is the offset (in degrees) between them. The aperture size refers to the chopping aperture diameter. Variance in demodulation parameters is due to the microscope alignments. High-resolution images were acquired using a higher frequency to increase the electron counts to reduce drift.

Table S1. List of modulation and demodulation parameters for each pulsed beam image.

Figure	K1 (V)	K2 (V)	Phase (°)	Frequency (GHz)	Aperture Size (µm)
1c	0.3	0.06	57	2.6	25
2b	0.3	0.06	71	2.6	25
2c	0.3	0.05	81	2.6	25
3e	0.3	0.06	53	2.6	25
4d/4e	0.15	0.03	-156	3	25
5d/5e	0.2	0.04	30	2.6	25
6d (inset)	0.3	0.06	41	2.6	25
S1a	0.3	0.06	57	2.6	25
S3a/S3b	0.3	0.06	83	2.6	25
S5a/S5b	0	0	0	N/A	None
S5c	0.3	0	0	2.6	None
S5d	0.3	0.05	24	2.6	None
S5e	0.3	0	0	2.6	25
S5f	0.3	0.05	24	2.6	25

References:

[1] M. Fauver, E.J. Seibel, J.R. Rahn, M.G. Meyer, F.W. Patten, T. Neumann, A.C. Nelson,

Three-dimensional imaging of single isolated cell nuclei using optical projection tomography, Opt. Express. 13 (2005) 4210. https://doi.org/10.1364/opex.13.004210.
[2] X. Fu, E. Wang, Y. Zhao, A. Liu, E. Montgomery, V.J. Gokhale, J.J. Gorman, C. Jing, J.W. Lau, Y. Zhu, Direct visualization of electromagnetic wave dynamics by laser-free ultrafast electron microscopy, Sci. Adv. 6 (2020) eabc3456. https://doi.org/10.1126/sciadv.abc3456.